Available online at www.sciencedirect.com
ScienceDirect
Geochimica et Cosmochimica Acta 72 (2008) 360–377
Geochimica et Cosmochimica Acta
www.elsevier.com/locate/gca

Scale dependence of mineral dissolution rates within single pores and fractures

Li Li *, Carl I. Steefel, Li Yang

Earth Sciences Division, Lawrence Berkeley National Laboratory, 1 Cyclotron Road, Mail Stop 90-1116, Berkeley, CA 94720, USA

Received 22 May 2007; accepted in revised form 23 October 2007; available online 13 November 2007

Abstract

The possibility that gradients in concentration may develop within single pores and fractures, potentially giving rise to scale-dependent mineral dissolution rates, was investigated with experimentally validated reactive transport modeling. Three important subsurface mineral phases that dissolve at widely different rates, calcite, plagioclase, and iron hydroxide, were considered. Two models for analyzing mineral dissolution kinetics within a single pore were developed: (1) a Poiseuille Flow model that applies laboratory-measured dissolution kinetics at the pore or fracture wall and couples this to a rigorous treatment of both advective and diffusive transport within the pore, and (2) a Well-Mixed Reactor model that assumes complete mixing within the pore, while maintaining the same reactive surface area, average flow rate, geometry, and multicomponent chemistry as the Poiseuille Flow model. For the case of a single fracture, a 1D Plug Flow Reactor model was also considered to quantify the effects of longitudinal versus transverse mixing. Excellent agreement was obtained between results from the Poiseuille Flow model and microfluidic laboratory experiments in which pH 4 and 5 solutions were flowed through a single 500 μm diameter by 4000 μm long cylindrical pore in calcite. The numerical modeling and time scale analysis indicated that rate discrepancies arise primarily where concentration gradients develop under two necessary conditions: (1) comparable rates of reaction and advective transport, and (2) incomplete mixing via molecular diffusion. For plagioclase and iron hydroxide, the scaling effects are negligible at the single pore and fracture scale because of their slow rates. In the case of calcite, where dissolution rates are rapid, scaling effects can develop at high flow rates from 0.1 to 1000 cm/s and for fracture lengths less than 1 cm. Under more normal flow conditions where flow is usually slower than 0.001 cm/s, however, mixing via molecular diffusion is effective in homogenizing the concentration field, thus eliminating any discrepancies between the Poiseuille Flow and the Well-Mixed Reactor model. The analysis suggests that concentration gradients are unlikely to develop within single pores and fractures under typical geological/hydrologic conditions, implying that the discrepancy between laboratory and field rates must be attributed to other factors.
Published by Elsevier Ltd.

1. INTRODUCTION

The dissolution of minerals plays a major role in various physical, chemical, and biological processes in nature. Mineral dissolution affects the formation of soils, influences the degradation of radioactive waste and its containers (Spycher et al., 2003) and the subsequent migration of heavy metals and radionuclides to the biosphere (Lovley, 1993; Lovley and Coates, 1997; Chorover et al., 2003), and at larger space and time scales, it regulates the atmospheric concentrations of CO_2 (Berner, 1995; Berner and Berner, 1997). Laboratory-measured dissolution rates of many minerals have been consistently found to be several orders of magnitude faster than those observed in the field (White and Brantley, 2003; Maher et al., 2004), although it is not clear in all cases that this represents a true discrepancy in the rate constants as opposed to a failure to take into account the intrinsic differences in chemical and/or physical conditions between laboratory and field settings (Steefel et al., 2005).

* Corresponding author. Fax: +1 510 486 5686.
E-mail address: lili@lbl.gov (L. Li).
URL: http://esd.lbl.gov/ESD_staff/li_li (L. Li).

0016-7037/$ - see front matter Published by Elsevier Ltd.
doi:10.1016/j.gca.2007.10.027

Such rate discrepancies need to be resolved, however, since they seriously hinder the application of laboratory-measured dissolution rates to natural systems.

A variety of factors have been proposed to contribute to the discrepancies between laboratory and field rates, including the differences in reactive surface area of the fresh and weathered minerals (White and Peterson, 1990; Anbeek, 1993; White, 1995), the effect of reaction affinity (White, 1995; White and Brantley, 2003; Maher et al., 2006), the precipitation rate of secondary clay minerals (Steefel and Van Cappellen, 1990; Alekseyev et al., 1997; Zhu et al., 2004; Maher et al., 2006), and the age of the reacting material (White and Brantley, 2003; Maher et al., 2004). Recent studies have also shown that physical and chemical heterogeneities in soils and aquifers where subsurface flow occurs may contribute to a scale dependence to mineral dissolution rates, and thus potentially to discrepancies between laboratory and field rates (Malmstrom et al., 2000, 2004; Li et al., 2006; Meile and Tuncay, 2006). For example, Li and coworkers (Li et al., 2006, 2007) found that variations in the spatial distributions of minerals with differing reactivity can result in the development of concentration gradients of chemical species involved in dissolution reactions, thus leading to erroneous predictions of reaction rates when the scale dependence is not accounted for. More generally, any chemical, physical, or microbiological heterogeneity that results in the formation of concentration gradients in the subsurface can lead to a scale dependence of the rates, and thus potentially to discrepancies between laboratory and field rates.

While the discrepancies between laboratory and field rates cannot be attributed entirely to the effect of physical and chemical heterogeneities, as indicated by studies of weathering rates in physically and chemically homogeneous media (Maher et al., 2006), it is clear that a comparison of lab and field rates requires careful consideration of the inherent differences between the laboratory and natural systems as suggested above. The laboratory measurement of dissolution rates usually employs well-mixed batch or flow through reactors. In these experimental systems, the aqueous phase is stirred rapidly enough that the aqueous phase becomes well-mixed, thus eliminating the effect of transport. In such cases, mineral dissolution is surface-controlled and depends only on the uniform chemistry of the aqueous solution. In natural systems, however, reactions are inevitably subject to the influence of transport via advection, molecular diffusion, and/or dispersion. As such, the mineral dissolution rates are an outcome of coupling between the reaction and transport processes.

In addition to these differences, natural porous or fractured media are also very different from laboratory settings in terms of their structure and heterogeneous nature. For example, natural porous media typically possess hierarchical structures and spatial scales that range from the pore scale, to the continuum scale, and finally to the field scale. The pore scale focuses on individual pores at the spatial scale of tens to thousands of microns, while the continuum scale, often at the scale of millimeters to centimeters, contains a sufficient number of pores that allows the definition of statistically averaged properties of porous media, including porosity and permeability (Bear, 1972). The field scale, often from meters to kilometers, is the scale at which we examine specific processes in natural field settings. Heterogeneities in the physical and chemical properties of porous media exist at all spatial scales. While at the continuum and field scales porous media are often represented by properties and processes "averaged" over a large number of pores, the pore scale is where processes such as flow, transport, and reactions actually take place. As such, pores are the fundamental building blocks of natural porous media and are an important starting point to examine the scaling issue with regard to reaction rates.

The effect of transport, especially diffusion, on mineral reaction rates in natural systems has been discussed previously in the context of transport-controlled versus surface-controlled reaction kinetics and the validity of the local equilibrium assumption (Berner, 1978; Dibble and Tiller, 1981; Casey, 1987; Murphy et al., 1989). These studies did not address the detailed flow patterns developed in single pores and fractures and focused primarily on single component systems so that analytical solutions could be derived for the time evolution of the aqueous concentrations. In this work, we examine the effects of advective and diffusive transport on mineral dissolution that involve multiple species in single pores and fractures, where flow can no longer be described completely by an average Darcy velocity—gradients in flow velocity inevitably exist within individual pores as a result of the fundamental physics. Such flow gradients, as well as the limited rates of diffusive transport, can present conditions where reactions are limited by flow and transport, which are very different from conditions in well-mixed batch or flow through reactors in laboratory settings. We aim to understand the mechanisms that contribute to the rate discrepancies between laboratory and field settings at the single pore and fracture scale and to identify the conditions under which such rate discrepancies become significant.

In this study, laboratory-measured reaction kinetics are applied at the scale of the mineral–water interface where they occur, and then coupled with a rigorous treatment of flow and transport. Although the model for a single pore is highly idealized in terms of its geometry, first-order effects in terms of the coupling of flow, transport, and reaction kinetics are captured. The numerical model used here for flow and transport is verified with an analytical solution. In addition, the coupled representation of flow, transport, and reaction by the model is validated with a microfluidic reactive flow experiment carried out at a spatial scale of hundreds to thousands of microns. We then compare rates within the single pores and fractures obtained from these fully coupled reactive transport simulations to rates obtained from a model that assumes complete mixing within the pore, while maintaining the same reactive surface area, average flow rate, geometry, and multicomponent chemistry.

For single fractures, the effect of transverse mixing is evaluated by comparing the rates from the fully coupled 2D reactive transport simulations to those calculated from a 1D plug flow reactor model that assumes complete transverse mixing within the fracture. The comparisons were

made under various flow, pore size, and fracture length conditions to identify and quantify the conditions under which gradients in concentration (and thus, in rates) may develop.

2. REACTIONS AND RATE LAWS

In this work, we focus on the dissolution of three important subsurface mineral phases with a range of reaction rates: calcite, plagioclase, and iron hydroxide. Calcite dissolution is one of the most important and rapid mineral reactions in the subsurface (Morse and Arvidson, 2002), while plagioclase dissolution is one of the slowest, with its rate about 5–6 orders of magnitude less than that of calcite (Blum and Stillings, 1995; White and Brantley, 1995). Dissimilatory iron reduction is an example of a dissolution reaction with an intermediate rate, and is one of the most important biogeochemical reactions in the environment where it affects nutrient cycling and the fate of many subsurface contaminants (Lovley and Coates, 1997; Coates and Anderson, 2000; Anderson et al., 2003).

2.1. Calcite dissolution

The dissolution of calcite has been proposed to occur via three parallel reactions (Plummer et al., 1978; Chou et al., 1989):

$$CaCO_3(s) + H^+ \iff Ca^{2+} + HCO_3^- \quad (1)$$

$$CaCO_3(s) + H_2CO_3^* \iff Ca^{2+} + 2HCO_3^- \quad (2)$$

$$CaCO_3(s) \iff Ca^{2+} + CO_3^{2-} \quad (3)$$

The reaction consumes H^+, and releases Ca^{2+} and carbonate. In the model, the rate of calcite dissolution is described by a Transition State Theory (TST) rate law, with the reaction rate parameters determined by Chou et al. (1989):

$$\text{Rate} = A(k_1 a_{H^+} + k_2 a_{H_2CO_3^*} + k_3)\left(1 - \frac{\text{IAP}}{K_{eq}}\right), \quad (4)$$

where k_1, k_2, and k_3 are the reaction rate constants, a_{H^+} and $a_{H_2CO_3^*}$ are the activities of hydrogen ion and carbonic acid, IAP is the ion activity product defined as $a_{Ca^{2+}} a_{CO_3^{2-}}$, K_{eq} is the equilibrium constant for the reaction, and A is the reactive surface area. The values of k_1, k_2, and k_3 at 25 °C are 0.89, 5.01×10^{-4}, and 6.6×10^{-7} mol m^{-2} s^{-1}, respectively (Chou et al., 1989). The reaction rate is pH-dependent under acidic conditions and becomes almost constant above a pH of about 7 (Fig. 2 in Chou et al., 1989).

2.2. Plagioclase dissolution

Our model plagioclase, which contains 70% anorthite (labradorite), dissolves under slightly acidic conditions according to the following reaction

$$Ca_{0.7}Na_{0.3}Al_{1.7}Si_{2.3}O_8 + 1.2H_2O + 6.8H^+ \iff 0.7Ca^{2+} + 0.3Na^+ + 1.7Al^{3+} + 2.3H_4SiO_4 \quad (5)$$

The dissolution of plagioclase has been described by several rate laws in the literature. To examine the possible effect of the form of reaction rate laws on the scaling behavior of reaction rates, we consider two separate rate laws in this work. The first is an aluminum inhibition rate law (Oelkers et al., 1994) that describes the dependence of the dissolution rate on pH and aluminum concentration,

$$\text{Rate} = Ak\left(\frac{K'_f}{a_{Al(OH)_3}{}^{1/3} + K'_f}\right)\left(1 - \left(\frac{\text{IAP}}{K_{eq}}\right)^{1/3}\right), \quad (6)$$

here rewritten following Maher et al. (2006). In Eq. (6), k is the reaction rate constant, K'_f is the formation constant for a silica-rich surface complex involved in the rate-limiting step in the overall dissolution reaction, which has a value of 1.50×10^{-5}, and IAP is the ion activity product. The rate constant k for plagioclase containing 70% anorthite is estimated to be 1.12×10^{-9} mol m^{-2} s^{-1} at 25 °C, which is extrapolated from a rate constant measured for a plagioclase containing 60% anorthite (Carroll and Knauss, 2005) using a correlation between reaction rate constants and plagioclase composition (Blum and Stillings, 1995). The logarithm of the equilibrium constant is 19.28 for a plagioclase containing 70% anorthite (Stefansson, 2001).

The second rate law considered is one proposed by Hellmann and Tisserand (2006) that describes the dependence of the rate on reaction affinity or Gibbs free energy, and is similar to one proposed earlier for albite (Burch et al., 1993) for albite. This dependence is combined with the pH dependence described in Blum and Stillings (1995) under far from equilibrium conditions. For a Ca-rich plagioclase, the rate dependence on pH is raised to the power of 0.72, giving the following overall reaction rate law:

$$\text{Rate} = A\{k_1 a_{H^+}{}^{0.72}[1 - \exp(-ng^{m_1})] + k_2 a_{H^+}{}^{0.72}[1 - \exp(-g)]^{m_2}\}, \quad (7)$$

where g is equal to $|\Delta G_r|/RT$, with ΔG_r being the Gibbs free energy of the reaction, R the gas constant, and T the temperature in degrees Kelvin. The parameters k_1 and k_2 are reaction rate constants at 25 °C estimated to be 4.08×10^{-9} and 7.19×10^{-11} mol m^{-2} s^{-1}, respectively, based on the plagioclase dissolution rate under far from equilibrium conditions (Blum and Stillings, 1995), the ratios of these two values in Hellmann and Tisserand (2006), and a temperature correction using an activation energy of 15.0 kcal/mol. The values of n, m_1, and m_2 are 7.98×10^{-5}, 3.81, and 1.17 (Hellmann and Tisserand, 2006).

2.3. Dissimilatory dissolution of iron hydroxide

Assuming acetate as the electron donor, dissimilatory reductive dissolution of an iron hydroxide like goethite proceeds as follows:

$$FeOOH(s) + \frac{1}{8}CH_3COO^- + \frac{15}{8}H^+ \iff Fe^{2+} + \frac{1}{4}HCO_3^- + \frac{3}{2}H_2O. \quad (8)$$

The dependence of the rate on acetate is usually described by a Monod term. For goethite, however, recent studies have shown that the rate of iron reduction also depends on the surface area and the concentration of surface sites available for reaction (Roden and Zachara, 1996; Liu

et al., 2001; Jaisi et al., 2007), which can be inhibited due to the adsorption of Fe(II) on the goethite surface (Roden et al., 2000; Roden and Urrutia, 2002; Roden, 2004). Accordingly, we use the following rate law that combines a dependence on acetate concentration and on available iron hydroxide surface sites:

$$\text{Rate} = V_{\max,\text{Fe(III)}} \frac{c_{\text{acetate}}}{K_{\text{s,acetate}} + c_{\text{acetate}}} [> \text{FeOH}]_{\text{available}}, \quad (9)$$

where $V_{\max,\text{Fe(III)}}$ is the maximum surface-area-normalized rate of iron reduction, with a value of 1.655×10^{-6} mol (mole sites)$^{-1}$ s^{-1} (Scheibe et al., 2006), c_{acetate} is the aqueous concentration of acetate (mol/L), $K_{\text{s,acetate}}$ is the half-saturation constant of acetate, with a value of 10^{-4} mol/L (Scheibe et al., 2006), and $[>\text{FeOH}]_{\text{available}}$ is the available surface site density of iron hydroxide in units of (mole sites) m^{-2}. The value of $[>\text{FeOH}]_{\text{available}}$ is equal to $[> \text{FeOH}_s] + [> \text{FeOH}_w] - [> \text{FeOFe}^+{}_s] - [> \text{FeOFe}^+{}_w]$, which is the summation of total strong and weak iron surface site densities ($[>\text{FeOH}_s]$ and $[>\text{FeOH}_w]$, respectively), subtracted by the densities of sites occupied by the adsorbed Fe(II) ($[> \text{FeOFe}^+{}_s]$and$[> \text{FeOFe}^+{}_w]$). The density of strong and weak iron surface sites are taken as 9.27×10^{-8} and 3.70×10^{-6} (mol sites) m^{-2} (Appelo et al., 2002), respectively. The adsorption of Fe(II) on iron hydroxide surface is modeled using a surface complexation model based on the electrical double layer theory (Dzombak and Morel, 1990), with parameters from Appelo et al. (2002):

$$> \text{FeOH}_s + \text{Fe}^{2+} = > \text{FeOFe}_s^+, \quad \log K = -0.95, \quad (10)$$

$$> \text{FeOH}_w + \text{Fe}^{2+} = > \text{FeOFe}_w^+, \quad \log K = -2.98. \quad (11)$$

According to this rate law, as the Fe(II) concentration in solution increases with the progress of the reaction, the concentrations of the sorbed species $> \text{FeOFe}^+{}_s$ and $> \text{FeOFe}^+{}_w$ increase as well, thus effectively inhibiting the rate of dissolution.

2.4. Incorporation of aqueous speciation

Since the mineral dissolution rates calculated using the rate laws given above depend on the detailed multicomponent chemistry, aqueous complexation reactions were also included as well. A full list of the relevant complexes and their equilibrium constants are given in Table 1. For the calcite system, the relevant aqueous species considered include H^+, Na^+, Cl^-, Ca^{2+}, CO_2(aq), HCO_3^-, CO_3^{2-}, $CaOH^+$, HCl(aq), OH^-, $CaCO_3$(aq), $CaCl^+$, $CaCl_2$(aq). The equilibrium constants for the aqueous speciation reactions are from the EQ3/6 database. All calculations are carried out with the code CrunchFlow (Steefel, 2008 and www.csteefel.com).

Table 1
Aqueous complexation reactions involved in modeling the three kinetic reactions and equilibrium constants from EQ3/6 database[a]

Kinetic reactions	Aqueous complexation reactions	$\log K_{eq}$
Calcite dissolution	$H_2O = H^+ + OH^-$	−13.99
	$H_2CO_3(aq) = H^+ + HCO_3^-$	−6.34
	$H_2CO_3(aq) = 2H^+ + CO_3^{2-}$	−10.32
	$Ca^{2+} + OH^- = CaOH^+$	−12.85
	$Ca^{2+} + HCO_3^{2-} = CaCO_3(aq) + H^+$	−7.01
	$Ca^{2+} + Cl^- = CaCl^+$	−0.70
	$Ca^{2+} + 2Cl^- = CaCl_2(aq)$	−0.65
	$Ca^{2+} + HCO_3^- = CaHCO_3^+$	10.43
	$H^+ + Cl^- = HCl(aq)$	0.70
Plagioclase dissolution	$H_2O = H^+ + OH^-$	−13.99
	$H_2CO_3(aq) = H^+ + HCO_3^-$	−6.34
	$H_2CO_3(aq) = 2H^+ + CO_3^{2-}$	−10.32
	$Ca^{2+} + OH^- = CaOH^+$	−12.85
	$Ca^{2+} + HCO_3^{2-} = CaCO_3(aq) + H^+$	−7.01
	$Ca^{2+} + Cl^- = CaCl^+$	−0.70
	$Ca^{2+} + 2Cl^- = CaCl_2(aq)$	−0.65
	$Ca^{2+} + HCO_3^- = CaHCO_3^+$	10.43
	$H^+ + Cl^- = HCl(aq)$	0.70
	$H_4SiO_4 = 2H^+ + H_2SiO_4^{2-}$	−22.96
	$HSiO_3^- = SiO_2(aq) + OH^-$	9.94
	$Al(OH)_3(aq) = Al^{3+} + 3OH^-$	−25.57
	$Al(OH)_3(aq) = AlOH^{2+} + 2OH^-$	−16.53
	$Al(OH)_3(aq) = Al(OH)_2^+ + OH^-$	−8.16
	$Al(OH)_3(aq) = AlO(OH)_2^- + H^+$	−6.45
	$NaCl(aq) = Na^+ + Cl^-$	0.78
	$NaHCO_3(aq) = Na^+ + HCO_3^-$	−0.16
	$NaHSiO_3(aq) = Na^+ + HSiO_3^-$	8.30
Iron hydroxide dissolution	$H_2O = H^+ + OH^-$	−13.99
	$H_2CO_3(aq) = H^+ + HCO_3^-$	−6.34
	$H_2CO_3(aq) = 2H^+ + CO_3^{2-}$	−10.32
	Acetic_acid $= H^+ +$ Acetate	−4.75
	$FeCl^+ = Fe^{2+} + Cl^-$	0.16
	$FeCl_2(aq) = Fe^{2+} + 2Cl^-$	2.46
	$FeOH^+ = Fe^{2+} + OH^-$	9.50
	$H^+ + Cl^- = HCl(aq)$	0.70
	$NaCl(aq) = Na^+ + Cl^-$	0.78

[a] The standard state adopted in this study is that of unit activity for pure minerals and H_2O at any temperature and pressure. For aqueous species other than H_2O, the standard state is unit activity of the species in a hypothetical 1 molal solution referenced to infinite dilution at any temperature and pressure.

3. MODELS FOR SINGLE PORES AND FRACTURES

3.1. Model for a single pore

To analyze the scale dependence of mineral dissolution rates at the pore scale, we developed two models: (1) a *Poiseuille Flow* model that applies laboratory-measured dissolution kinetics at the pore or fracture wall and couples this to a rigorous treatment of both advective and diffusive transport, and (2) a *Well-Mixed Reactor* model that assumes complete mixing within the pore, while maintaining the same reactive surface area, average flow rate, geometry, and multicomponent chemistry as the Poiseuille Flow model. The Poiseuille Flow model is considered as the more realistic representation of the actual processes taking place in the pore, while the Well-Mixed Reactor model is used as a means of quantifying the extent to which concentration gradients within a single pore affect the averaged reaction rates.

3.1.1. Poiseuille Flow model

In this model, pores are assumed to be cylindrical. Assuming Poiseuille's equation for flow in a cylinder holds, the steady-state parabolic velocity distribution within the pore as a

function of radial distance r from the center of the pore can be calculated as follows (Daugherty and Franzini, 1965):

$$u(r) = 2U\left[1 - \left(\frac{r}{R}\right)^2\right], \tag{12}$$

where r is the position in radial coordinates, $u(r)$ is the local fluid velocity within the cylinder, U is the average flow velocity, and R is the radius of the cylinder. As such, the local flow is fastest at the radial center of the pore and zero at the pore wall. In the model, dissolution occurs only at the pore wall, which is made up of one of the three minerals: calcite, plagioclase, or iron hydroxide. The laboratory-determined rate laws, such as the rate law of Chou et al. (1989) for calcite dissolution, only apply within the grid cells (measuring 1.0 μm in width) containing the cylinder wall, that is, at the mineral–water interface where the reactions actually take place. The local reactive surface area is calculated from the geometry of the pore, with $A_{\text{grid}} = 2\pi R\Delta y$, where Δy is the grid spacing in the axial direction. Thus, the total surface is $A_{\text{tot}} = 2\pi RL$, where L is the length of the pore. This assumption could either overestimate the surface area, as in the case where the pore wall is not made up exclusively of one mineral or some of the surface is armored, or it could underestimate it by not including roughness of the mineral surface. The dissolution at the pore wall, coupled with a rigorous representation of the flow and diffusive transport, captures the dynamic reactive transport processes within a pore, even if the geometry is highly idealized. Reaction products from dissolution are swept and diffused downstream in the y (axial) direction, but also radially toward the center of the pore via molecular diffusion (Fig. 1a).

The model was implemented in the numerical code CrunchFlow, a software for modeling multicomponent reactive flow and transport that has been applied to understand many complex (bio)geochemical systems (Giambalvo et al., 2002; Steefel et al., 2003; Knauss et al., 2005; Maher et al., 2006; Steefel, 2008). Details of the numerical model implementation are discussed more generally in Steefel and MacQuarrie (1996). For this work the global implicit approach (GIMRT) was used, which is adequate for steady-state systems like the one considered here (Steefel and MacQuarrie, 1996). All simulations were carried out with sufficiently fine grids that further refinement did not change the results, although further verification of the model's ability to capture the combination of the parabolic velocity field and molecular diffusion is provided below.

Multicomponent molecular diffusion is treated in CrunchFlow as a combination of Fickian diffusion of individual species and an electrochemical migration term arising from the diffusion of charged species at differing rates (Newman, 1991; Oelkers, 1996; Lasaga, 1998; Giambalvo et al., 2002; Maher et al., 2006; Steefel, 2007). The diffusion coefficients are taken from the table given in Lasaga (1998). Hydrodynamic dispersion is not considered as a separate process, since this effect is captured rigorously through the combination of the parabolic velocity field and molecular diffusion (Taylor, 1953). The flow field was calculated from Eq. (12) and then read into CrunchFlow, which was run with cylindrical coordinates.

Due to the coupling between flow, transport, and reactions, the aqueous concentrations at the outlet can vary as a function of radial distance. The averaged outlet concentration can be calculated by weighting the local concentrations by the local volumetric flux $Q(r)$ as follows:

$$c_{\text{out}} = \frac{\int_0^R \mathrm{c}(r)Q(r)}{Q_{\text{tot}}}. \tag{13}$$

Here c_{out} is the flux-weighted average concentration at the pore outlet, and $\mathrm{c}(r)$ is the concentration at radial distance r. The term $Q(r)$ is the volumetric flux at radial distance r, which is defined as $u(r) \times 2\pi r\mathrm{d}r$, the product of local flow velocity $u(r)$ and the radial cross-sectional area $2\pi r\mathrm{d}r$. The total flow rate Q_{tot} is defined by

$$Q_{\text{tot}} = \int_o^R Q(r) = \int_o^R u(r) \times 2\pi r\mathrm{d}r. \tag{14}$$

The averaged outlet concentration depends on local dissolution rates at the pore wall, the advective transport along the axis of the pore, and the diffusive transport in both the axial and transverse directions. The overall reaction rate within the pore, $R_{2\text{D}}$, is calculated from the flux-weighted average of concentrations in the outlet solution, that is, the effluent chemistry. Based on the mass balance of the pore, the averaged area-normalized dissolution rate within the pore at steady-state $R_{2\text{D}}$ can be calculated as follows:

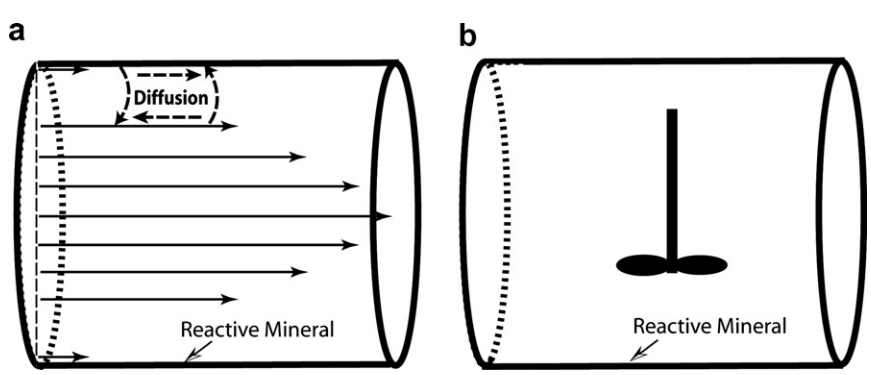

Fig. 1. (a) Conceptual model for the Poiseuille Flow model, which considers reactive flow and transport in a single axi-symmetric cylindrical pore. The velocity profile is taken from the analytical solution for Poiseuille flow in a cylinder (Daugherty and Franzini, 1965). (b) Conceptual model for the Well-Mixed Reactor model. Comparison of the rates from the two models quantifies the effects of mixing through molecular diffusion in both the transverse and longitudinal directions.

$$R_{2D} = \frac{(c_{out} - c_{in})Q_{tot}}{\nu A_{tot}}, \quad (15)$$

where c_{in} is the inlet concentration, and ν is the stoichiometric coefficient of the species for the mineral of interest that is used to calculate the average rate. Like the concentration field, the value of R_{2D} is also a function of coupling between flow, transport, and dissolution at the pore wall. The value of R_{2D} is equivalent to the dissolution rate integrated over the entire pore wall and normalized by total available surface area.

While a cylindrical pore is an idealized model of a natural pore, it captures the important first order effects, including the fact that flow is slower close to the mineral surface, an important feature of transport within a pore that affects the extent of mixing. In single pores, the conditions under which concentration gradients develop depend on the relative rates of flow, transport, and reactions. In the case where the reaction rate is fast enough relative to transport to change the aqueous chemistry of the pore, the tendency to develop concentration gradients within the pore depends on the effectiveness of molecular diffusion relative to flow—where flow is sufficiently rapid compared to molecular diffusion over the length scales of the single pore, concentrations within the pore will not be uniform and dissolution rates depend on the scale over which the concentration, and thus the reaction rate, are averaged.

3.1.2. Well-Mixed Reactor model

A Well-Mixed Reactor model for a single pore (Fig. 1b) is developed for comparative purposes so as to quantify the extent to which concentration gradients captured by the Poiseuille Flow model affect the averaged reaction rates within a single pore. The pore represented in the Well-Mixed Reactor model possesses the same physical and chemical properties as that of the Poiseuille Flow pore, including total volume, reactive surface area, and total flow rate, except for the assumption that a rapid mixing rate ensures that there is no diffusion limitation on the rate—thus, the rate, R_M, is equivalent to what would be the case *if* the single pore behaved as a well-stirred laboratory reactor (Fig. 1b). Under such conditions, the rate can be calculated from the laboratory-measured rate law using the equations in Section 2 and the uniform concentrations within the well-mixed pore.

The ratio of the rate from the well-mixed model, R_M, over R_{2D} is used to quantify the discrepancy in overall rate between a well-mixed reactor and a natural pore. A ratio close to one indicates that the discrepancy in rates is negligible, that is, the pore is behaving effectively as a well-mixed reactor. In contrast, a ratio significantly different from one implies that rates in natural pores and well-mixed reactors are not the same.

3.2. Models for a single fracture

Since the length of a single fracture can be considerably longer than the width of its aperture (in contrast to the geometry of a single pore), the effects of transverse and longitudinal mixing need to be assessed separately. As such, we consider an additional model, a 1D Plug Flow Reactor model, which is designed to quantify the effect of transverse mixing within the fracture. The other two, the Poiseuille Flow and Well-Mixed Reactor models differ only geometrically from those considered for the cylindrical pore described above.

3.2.1. Poiseuille Flow model

Conceptually, single fractures are represented by two parallel plates. The distance between the two plates is the fracture aperture. The flow field within a fracture is represented by the Poiseuille flow between two parallel plates:

$$u(x) = 1.5U\left[1 - \left(\frac{x}{\delta}\right)^2\right], \quad (16)$$

where x is the transverse distance to the center of a fracture with the origin being the center of the aperture, $u(x)$ is the local fluid velocity within the fracture, U is the average flow velocity, and δ is the half fracture aperture. As in the case of the single pore model, dissolution occurs only at the fracture wall itself.

By discretizing the fracture in both the transverse and longitudinal directions, we make no a priori assumption about the extent of mixing in either direction. The extent of mixing is determined by molecular diffusion, which is calculated numerically within the model. As with the cylindrical pore, dispersion is not explicitly considered in the model, other than by the combination of the detailed parabolic flow field and the longitudinal and transverse molecular diffusion. Overall reaction rates (R_{2D}) are calculated from the flux-weighted average of outlet concentrations in a similar fashion to the single pore model (Eq. (15)).

3.2.2. 1D Plug-Flow Reactor model

The fracture can also be represented by a 1D Plug-Flow Reactor model in which the longitudinal direction is discretized, while complete mixing in the transverse direction is assumed. The result is a 1D model that does not consider the parabolic velocity profile within the fracture. Overall rates from the 1D model (R_{1D}) are calculated from the concentrations of outlet solution (in this model, now represented by a single grid cell, in contrast to the 2D case). Comparison between R_{2D} and R_{1D} quantifies the effects of transverse mixing.

3.2.3. Well-Mixed Reactor model

The fracture here is represented by the Well-Mixed Reactor model assuming complete mixing in both transverse and longitudinal directions. The overall rates (R_M) are also calculated from the difference between concentrations of influent and effluent. Comparison between R_{2D} and R_M provides a measure of the combined effects of transverse and longitudinal mixing, while comparison between R_{1D} and R_M provides a measure of the effects of longitudinal mixing.

4. VALIDATION AND VERIFICATION OF THE POISEUILLE FLOW MODEL

4.1. Verification of transport for a cylindrical pore

The numerical model implemented in CrunchFlow is verified against an analytical solution for Taylor dispersion

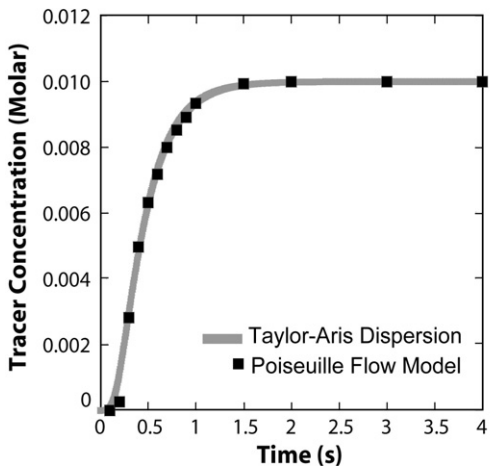

Fig. 2. Comparison of non-reactive tracer breakthrough curves calculated with a 1D geometry using an analytical Taylor-Aris dispersion coefficient (Taylor, 1953) and a full 2D numerical calculation of transport in a cylinder using the code CrunchFlow.

(Taylor, 1953). Using Eq. (12) for the flow field within a cylindrical pore, Taylor derived an analytical expression for hydrodynamic dispersion (Taylor, 1953)

$$D_h = D + \frac{UR^2}{D}, \tag{17}$$

where D_h is the dispersion coefficient, and D is the molecular diffusion coefficient. Note that the molecular diffusion coefficient appears both in the first term on the right hand side of Eq. (17), where it contributes to dispersion in the longitudinal or axial direction, and in the denominator of the second term, where it counteracts the dispersion attributable to the variation in velocity within the pore.

Fig. 2 shows a comparison between the breakthrough curve for a non-reactive tracer calculated with a one dimensional geometry using the Taylor-Aris dispersion coefficient given in Eq. (17) and a 2D axi-symmetric cylindrical Poiseuille flow calculation where dispersion is represented explicitly through the variation in flow velocities and molecular diffusion. The excellent agreement indicates that the numerical code CrunchFlow captures the transport within the pore accurately.

4.2. Validation with a microfluidic reactive flow experiment

To validate the Poiseuille Flow model, a microfluidic reactive flow experiment was carried out using a 500 μm diameter and 4000 μm long cylindrical pore drilled in a single crystal of calcite (Fig. 3a). Single crystals of calcite (Iceland spar) were cut into 20 mm (L) by 10 mm (W) slabs and polished down to the thickness of 4 mm. A 500 μm diameter cylindrical pore was drilled through the center of the polished sample sandwiched between two protecting ceramic plates (100 μm thickness). Nanoport® assemblies (Upchurch Scientific) were attached to the protecting ceramic plates for transferring fluids in and out of the calcite single pore. Input solutions were prepared using deionized water (18.3 Mega-Ohm) equilibrated with atmospheric CO_2 and were adjusted to the desired pH with diluted ultrapure HNO_3 acid (J.T. Baker®). The ionic strength of input solutions was adjusted to 10 mM with reagent grade NaCl (Omnipure® from EMD). The output solution pH was measured with Orion® micro-pH electrode. All effluent samples were acidified with 2% ultrapure HNO_3 and analyzed in triplicate by inductive coupled plasma-optical emission spectrometer (ICP-OES, Perkin-Elmer 5300 DV model) with a micro-PFA nebulizer.

Solutions at pH 4 and 5 were injected into the pore with a syringe pump at two different flow rates, 4.72 and 9.39 μL/min. These flow rates result in average velocities within the pore of 0.04 and 0.08 cm/s, respectively. Note

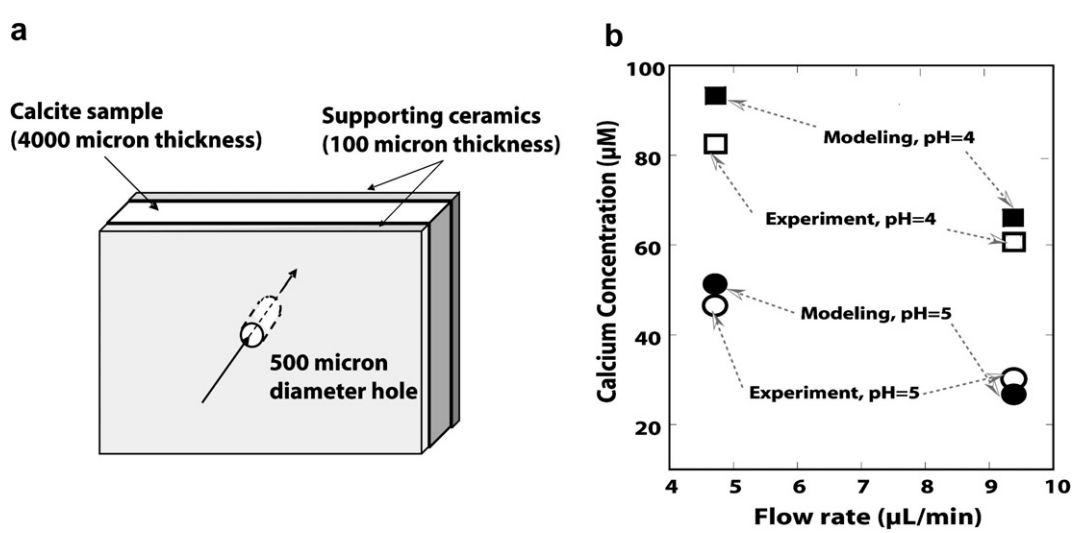

Fig. 3. (a) Schematic representation of the microfluidic reactive flow experiment. (b) Comparison of the flux-weighted average concentration of Ca^{2+} calculated from the numerical Poiseuille Flow model and the measured Ca^{2+} concentration from the outlet of the microfluidic reactive flow experiment under two pH and flow conditions. The numerical model uses a flow field based on Poiseuille's Law (Daugherty and Franzini, 1965) and a calcite dissolution rate law from Chou et al. (1989) that is applied at the mineral–water interface (the pore wall). The simulation results match the experimental data well, thus validating the numerical model.

that the reactive surface area is calculated in the grid cells along the cylinder wall from $A_{grid} = 2\pi R\Delta y$, where Δy is the grid spacing in the axial direction. The rate law given in Eq. (7) (Chou et al., 1989) is assumed to apply at the mineral–water interface, that is, within the grid cells containing the cylinder wall.

Fig. 3b compares the flux-weighted average concentration of Ca^{2+} calculated from the Poiseuille Flow model for the cylindrical pore to the measured Ca^{2+} concentration from the microfluidic experiment at steady-state under the two pH and flow conditions. The effluent solutions were collected after 15 min, or approximately 44 pore volumes. The agreement between the model and experimental results is excellent, indicating not only that the rate law (Chou et al., 1989) is applicable in this case, but also that the choice of a total reactive surface area of $A_{tot} = 2\pi RL$ is appropriate. Experiments conducted with very low ionic strength water (deionized water adjusted only with nitric acid and without NaCl) gave rates that were considerably lower than these presented here (results not shown). The explanation for the lower rates in the case of the low ionic strength water is not known for certain, but it is likely the result of the slower rate of diffusion from the pore wall to the center of the pore because of the smaller gradient in chemical potential as compared to the 10 mM NaCl solution.

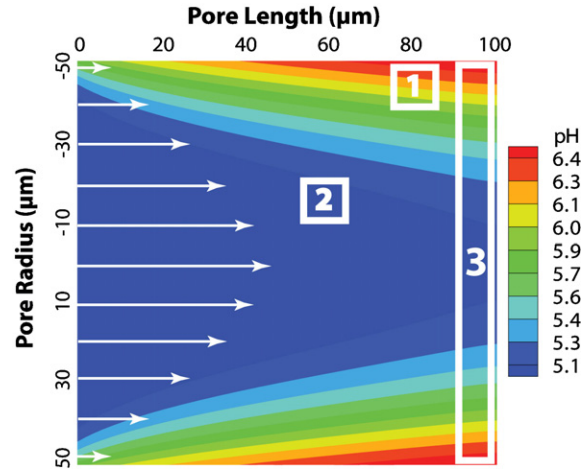

Fig. 4. Steady-state contour plot of pH for a cross-section of a pore of 100 μm in length and in diameter, with a pH 5 solution injected at a rate of 0.1 cm/s. The dissolution rate is scale-dependent, as is clear from comparing different sample volumes: Box 1 represents a micro-sample volume close to the pore wall showing a higher pH (and calcium concentration) than does Box 2 in the center of the pore, while Box 3, which averages the concentrations over the entire diameter of the pore, represents the pH that would be sampled as effluent.

5. RESULTS

5.1. Development of concentration gradients at the pore scale

To illustrate the effects of coupling between flow, transport, and reaction on the scale dependence of reaction rates (and thus to discrepancies between lab and field rates that may be due to processes operating at the pore scale), we show a steady-state concentration field that develops within a calcite pore of 100 μm in length at a flow velocity of 0.1 cm/s. The pore is infiltrated by a dilute pH 5 solution with 0.01 mM dissolved NaCl, equilibrated with atmospheric CO_2 gas. Under these slightly acidic conditions, the dissolution of the calcite raises the pH and calcium concentration in the solution. The increase in pH resulting from calcite dissolution has the effect of creating a wedge-shaped, higher pH zone in the direction of flow that broadens as a result of molecular diffusion (Fig. 4). Although not shown in Fig. 4, similar concentration gradients for other species, such as Ca^{2+} and H_2CO_3, also develop within the cylindrical pore. In this physical setting, if molecular diffusion were absent, the pH effects would be restricted to the immediate vicinity of the calcite surface along the pore wall.

Now as gradients in pH develop, it should be clear that the scale at which the solution in the pore is sampled determines the calcite dissolution rate that is calculated—for example, a microelectrode pH measurement from a small volume close to the calcite pore wall (Box 1 in Fig. 4) would indicate a dissolution rate greater than a pH measurement taken in a similarly sized volume in the center of the pore (Box 2 in Fig. 4). In the same way, a sample volume extending over the entire end of the pore (Box 3 in Fig. 4), as in the case where effluent from the entire pore is sampled, represents an average of a range of concentrations because of the gradients that develop. As a result, the bulk dissolution rate from the cylindrical pore, R_{2D}, calculated from the flux-weighted effluent concentration, does not necessarily represent the reaction progress in the immediate vicinity of the mineral surface, and therefore is scale-dependent.

5.2. Single pore results

To map out the conditions under which scale-dependent rates at the pore scale may develop, we modeled calcite, plagioclase, iron hydroxide dissolution under various hydrodynamic and pore size conditions. For all simulations, the pores were chosen to have equal values of diameter and length. Three pore sizes, 10, 100, and 1000 μm, were chosen that correspond to a range in size from relatively small pores in sandstones or clay-rich material (Acharya et al., 2005) to large pores in coarse-textured sediments or sandy soil (Khaleel and Relyea, 2001; Hwang and Powers, 2003; Khaleel and Heller, 2003). For each pore size, the pore flow velocity was varied from 10^5 to 10^{-5} cm/s to identify the conditions under which scaling effects become significant. The high flow velocities may be achieved in permeable aquifers in the vicinity of a pumping well, but otherwise are not common. All simulations were carried out at Reynolds numbers within the range of 10^{-7} to 10^3 below where turbulence typically begins.

In general, calcite dissolution rates in the Poiseuille Flow model and the Well-Mixed reactor model increase with increasing pore flow velocity, as shown in Fig. 5. With relatively slow flow velocities (slower than 0.1 cm/s), the long residence times allow diffusion to homogenize the concentration field, thus producing results that match those of the Well-Mixed Reactor model (see left panel of Fig. 5).

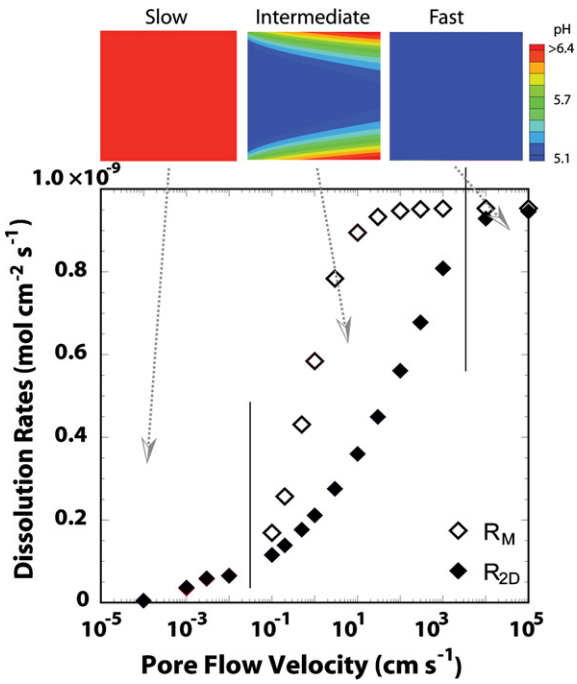

Fig. 5. Comparison of steady-state calcite dissolution rates calculated from the Poiseuille Flow model (R_{2D}) and those from the Well-Mixed Reactor model (R_M) as a function of the pore flow velocity for a pore of 100 μm in length and diameter. The upper panels show contour plots of pH for a cross-section of the pore under slow (left panel), intermediate (middle panel), and fast (right panel) flow velocities. Only under intermediate flow conditions where concentration gradients develop do the reaction rates depend on the spatial scale and the rate discrepancy between the two models reaches a maximum.

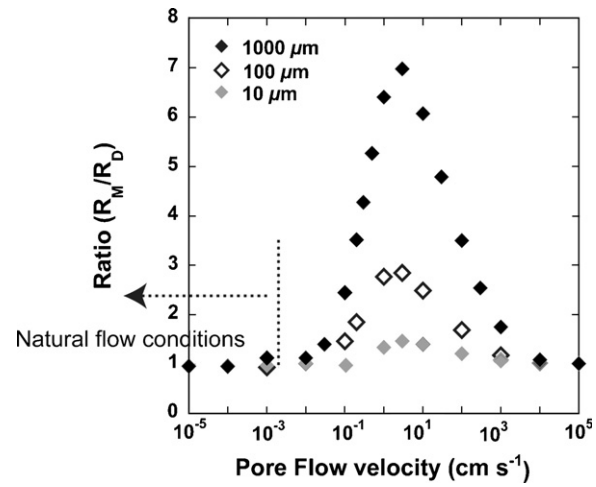

Fig. 6. The scaling effect in a single pore, quantified by the ratio of R_M/R_{2D}, under various flow conditions, and for three pore sizes, 1000, 100, and 10 μm. The scaling effects develop and are largest for flow velocities between 0.1 and 1000 cm/s, which are above the flow velocities encountered under natural conditions (typically slower than 0.001 cm/s).

With fast flow velocities (greater than 1000 cm/s), there is insufficient reaction to modify the pH even in areas close to the pore wall. This results in a uniform concentration field across the pore, again similar in this respect to the results from the Well-Mixed Reactor model (see right panel of Fig. 5). Only where reaction and advection rates are comparable, as is the case with moderate flow velocities, can large concentration gradients develop (as shown in the middle panel of Fig. 5). Under these conditions, the rate discrepancy between the two models is at its maximum.

Not surprisingly, the scaling effect, indicated by the deviation of the ratio of R_M over R_{2D} from unity, varies with flow velocity. At low and high flow velocities, the homogeneous concentration field makes the scaling effect negligible, with ratios of R_M over R_{2D} close to unity; under medium flow conditions, the scaling effect reaches a maximum. The scaling effect also increases with increasing pore size due to the lack of complete mixing within large pores, as shown in Fig. 6. With large pores (1000 μm), the ratio of R_M over R_{2D} can reach as high as 7, while with small pores (10 μm), the maximum ratio is only 1.3.

For both plagioclase and iron hydroxide pores, the pH profiles are uniform under all pore size and flow conditions, with pH values similar to that of the inlet solution. This is due to the fact that the dissolution rates of both plagioclase and iron hydroxide are so slow that their rates are much smaller than advection and diffusion under all conditions over the length scale of a single pore, thus leading to homogeneous concentration fields. The rate discrepancy at this scale is therefore negligible under all conditions in the case of these minerals.

At the pore scale, a discrepancy in flux-weighted average dissolution rate (obtained by applying Eqs. (13)–(15)) between the Poiseuille Flow model and the Well-Mixed Flow model occurs in the case of calcite under flow conditions between 0.1 and 1000 cm/s. Under natural flow conditions, however, the Darcy flow velocities are typically less than 0.001 cm/s. Although the flow velocities within individual pores can vary significantly due to the large variability in pore size, it is still uncommon for a pore flow velocity to be faster than 0.1 cm/s. As such, under natural conditions mixing via molecular diffusion is effective in homogenizing the concentration field, thus eliminating any discrepancies between the Poiseuille Flow and the Well-Mixed Reactor model. This suggests that a scale dependence to mineral dissolution rates is unlikely at the single pore or fracture scale under normal geological/hydrologic conditions, implying that the discrepancy between laboratory and field rates must be attributed to other factors.

5.3. Single fracture results

Although the size of fracture aperture can range from microns to hundreds of microns (Steefel and Lasaga, 1994), here we chose to examine a fracture of an intermediate aperture size of 100 μm, while its length is allowed to vary from tens of microns to one centimeter. This allows us to examine the extent to which fracture length affects any potential rate discrepancy. The flow conditions were chosen based on typical head gradients in field settings, permeability values for fractured rocks (Freeze and Cherry, 1979), and a fracture spacing of 0.1 m, which determine

the flow velocities varying from 10^{-1} to 10^{-5} cm/s. Here we detail the results for a flow velocity of 0.1 cm/s. The composition of the inlet solution is the same as that for the single pore simulations.

Fig. 7 shows the concentration fields for relevant species and pH for all three reactions for a fracture of 0.24 cm in length. Due to the fact that dissolution occurs at the fracture wall, concentrations of Ca^{2+} and Fe^{2+} are highest here and become progressively lower toward the center of the fracture. The contour plot of the Ca^{2+} and Fe^{2+} concentration fields look similar for all three reactions, since the geometry is determined primarily by the relative rate of flow and diffusion for a given fracture aperture, δ, or the Péclet number, given by Steefel and Lichtner (1998)

$$Pe = \frac{v\delta}{D}. \tag{18}$$

However, due to the significant differences in the magnitude of reaction rates, the extent of reaction is very different for the three reactions. With calcite dissolution, the Ca^{2+} concentration increases to about 10^{-5} mol/L, while for plagioclase and iron dissolution, the Ca^{2+} and Fe^{2+} concentrations only increase to about 10^{-9} mol/L. As a result, the pH values cover four pH units for calcite dissolution, while the pH change is negligible for both plagioclase and iron dissolution (on the order of 0.0001 to 0.001 pH unit), thus resulting in an essentially homogeneous pH field.

5.3.1. Calcite

The flux-weighted average calcite dissolution rates (again obtained from Eqs. (13)–(15)) from each of the three models decrease as the fracture length increases, as shown in Fig. 8a. This is largely due to the nonlinear coupling between dissolution rates and pH, as well as the associated spatial variation in dissolution rates along the fracture wall. The pH is lowest and therefore the dissolution rates are most rapid close to the fracture inlet. As mineral dissolution increases pH, it also decreases dissolution rates downstream, as can be seen from Fig. 9. Within a fracture of 0.24 cm in length, pH increases by more than four units and the dissolution rates drop almost an order of magnitude. Under these conditions, calcite dissolution is far from equilibrium. After pH reaches a value of about 7, the rate becomes constant because the rate is independent of pH, as indicated in Eq. (4). The result is that the surface-area normalized rates from the models decrease with increasing fracture length.

The ratios of the flux-weighted average calcite dissolution rates from the three models are also a function of the fracture length, as shown in Fig. 8b. As mentioned above, the ratio of R_{1D} over R_{2D} quantifies the effects of transverse mixing, the ratio of R_M over R_{2D} measures the combined effects of transverse and longitudinal mixing, while the ratio of R_M over R_{1D} indicates the effect of longitudinal mixing.

From Fig. 8b, it is interesting to notice that the effects of transverse mixing are much larger than the effects of longitudinal mixing, as the deviation of R_{1D}/R_{2D} from unity is much larger than that of R_M/R_{1D}. The assumption of complete transverse mixing in the 1D model leads to an overestimation of reaction rates by a factor of 3.3 in a 50 μm long fracture. The assumption of complete longitudinal mixing leads to an underestimation of reaction rates by a factor of 0.8 by the Well-Mixed Reactor model. As a result of the opposite direction of the effects of the transverse and longitudinal mix-

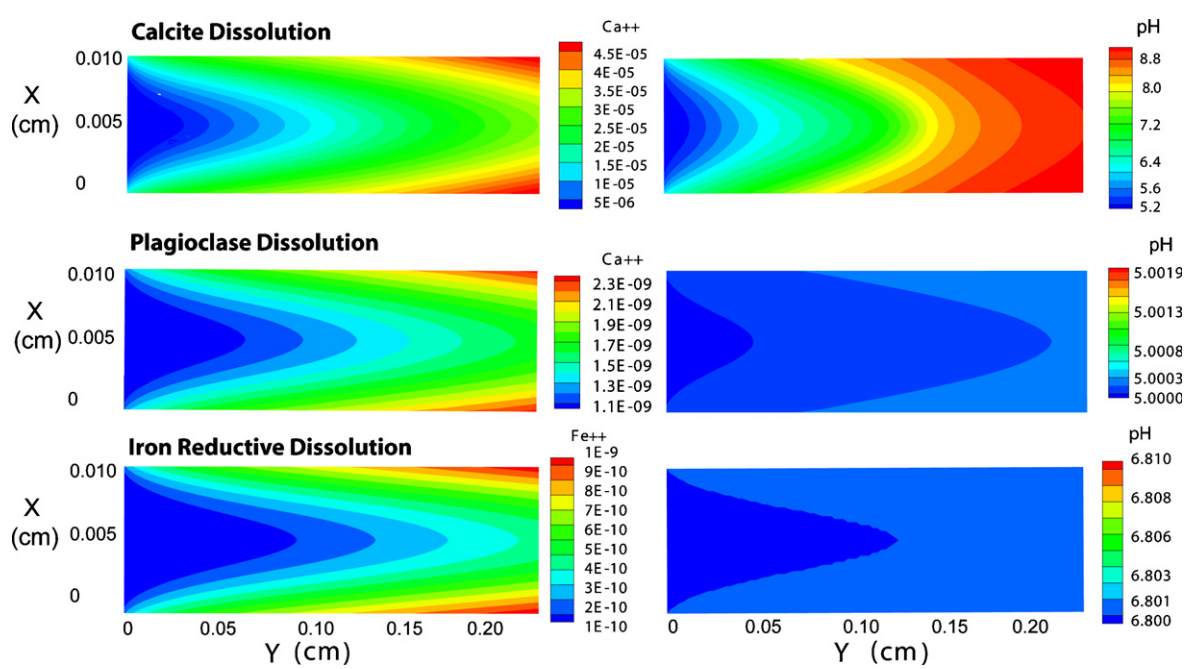

Fig. 7. Steady-state concentration fields of relevant species for calcite dissolution, plagioclase dissolution, and iron reductive dissolution in a fracture with an aperture of 100 μm and a length of 0.24 cm. The flow velocity is 0.1 cm/s. The Ca^{2+} and Fe^{2+} concentration fields look similar in terms of their shape, since this is determined by the relative rate of flow and diffusion. However, the extent of reaction differs significantly for the three minerals because of the difference in rates, an observation that is confirmed by the large change in pH values in the calcite fracture compared to the negligible pH change in the plagioclase and iron hydroxide fractures.

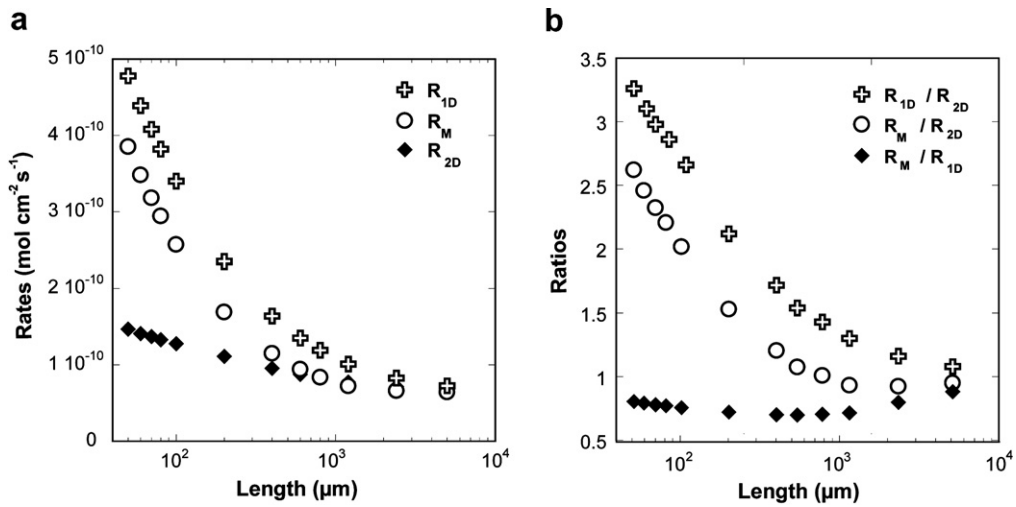

Fig. 8. (a) Flux-weighted average reaction rates at steady-state as a function of calcite fracture length, from the Poiseuille Flow model that fully couples the reactive transport processes (R_{2D}), the 1D Plug Flow Reactor model that assumes complete transverse mixing (R_{1D}), and the Well-Mixed Reactor model that assumes complete mixing in both longitudinal and transverse directions (R_M). (b) Comparison between steady-state flux-weighted average rates calculated from the three models. The ratio of R_{1D} over R_{2D} is a measure of the effects of transverse mixing; the ratio of R_M over R_{2D} is a measure of the combined effects of transverse and longitudinal mixing; and the ratio of R_M over R_{1D} indicates the effects of longitudinal mixing.

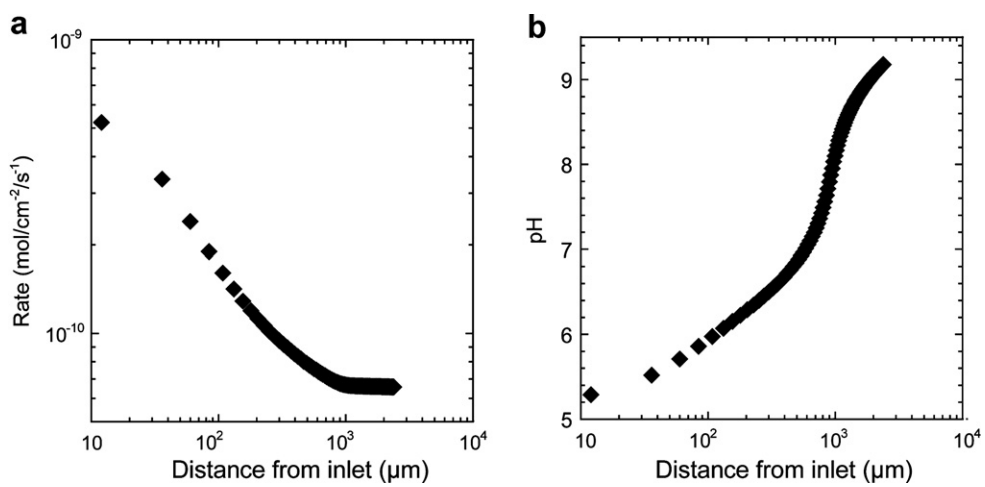

Fig. 9. Steady-state calcite dissolution rates (a) and pH (b) at the fracture wall as a function of distance from the inlet for a fracture of length 0.24 cm. Dissolution rates decrease rapidly close to the inlet due to the pH dependence and high reaction rates there. After the pH increases to about 7, dissolution rates become constant as the rate becomes independent of pH.

ing, the ratio of R_M over R_{2D}, which combines the two effects, falls in between the ratios of R_{1D}/R_{2D} and R_M/R_{1D}.

In all cases, the deviation from unity decreases with increasing length and the rates from the three models converge as longer fractures are considered. There are two reasons for this behavior. First, the fast dissolution rates at the fracture inlet leads to maximum concentration gradients in the transverse direction–while the Ca^{2+} concentration at the fracture wall is of the order of 10^{-5} mol/L, at the center of the fracture the Ca^{2+} concentration is almost zero, essentially the same as the inlet solution. As a result, most of the aqueous solution within a short fracture does not show significant reaction progress except in the immediate vicinity of the pore wall. With long fractures, however, molecular diffusion has more time to spread the Ca^{2+} from the fracture wall to its center, and the solution within the fracture becomes more nearly homogeneous. For example, at the outlet of a 0.24 cm long fracture, the Ca^{2+} concentrations at the fracture wall and the fracture center are of the same order of magnitude. Second, the dissolution rates at the fracture wall become constant once the fracture length is larger than 0.1 cm as a result of the increase in pH. Thus, scaling effects tend to diminish in the case of longer fractures.

This result suggests that for fast reactions such as calcite dissolution, the scaling effects can be large when the length scale of the fracture is small, and the scaling effects diminish with increasing fracture length. This is interesting in the

sense that it is different from the case of dispersion in hierarchical porous media, where scaling effects increase with increasing length scale (Gelhar et al., 1992).

5.3.2. Plagioclase

For plagioclase, the overall dissolution rates also decrease with increasing fracture length, as shown in Fig. 10a for rates calculated using aluminum inhibition rate law proposed by Oelkers et al. (1994). However, due to the slow plagioclase dissolution rate, there is little change in concentration and the fracture remains nearly homogeneous. As such, all three models give similar reaction rates, and the rate discrepancies are negligible compared to calcite dissolution, as shown in Fig. 10b. It is interesting to note that for plagioclase dissolution, the effects of transverse mixing are much smaller than those due to longitudinal mixing, as the ratios of R_{1D}/R_{2D} are all close to unity, while the ratios of R_M/R_{1D} deviates from unity slightly. This is primarily because plagioclase dissolution is so slow that significant concentration gradients do not develop in the transverse direction. It is also worth noting that the ratio of R_M/R_{1D} deviates from unity increasingly with increasing fracture length, meaning that the effects of longitudinal mixing become progressively more significant with increasing fracture length. This is particularly true for the aluminum inhibition rate law suggested by Oelkers et al. (1994), since complete mixing in the longitudinal direction results in higher aluminum concentrations close to the fracture inlet, and thus to slower overall rates. Simulations using the rate law proposed by Hellmann and Tisserand (2006) give similar results.

5.4. Time scale analysis

For an open geochemical system where flow, diffusive transport, and reactions are coupled, the time scales of these processes determine the dynamics of the system. Time scale analysis reveals that a scale dependence to reaction rates arises *only* when large concentration profiles develop, which occurs under two necessary conditions. First, diffusion must be slower than advection so that mixing is incomplete and does not homogenize the concentration field. Second, the rates of advection and reaction must be comparable so that the extent of reaction for the given residence time is large enough to produce significant concentration gradients within a pore or fracture. Both of these conditions must be satisfied to produce a discrepancy between the Poiseuille Flow model and a well-mixed system.

Quantitatively, the first condition means that the time scale of advection, τ_{ad}, is shorter than that of diffusion τ_{diff} ($\tau_{ad} < \tau_{diff}$). For a pore or fracture, however, values of τ_{diff} are different in the transverse and longitudinal directions. As a measure of the tendency to develop transverse concentrations gradients and assuming a pore or fracture with a characteristic length L and aperture δ, average flow velocity v, and diffusion coefficient D, the first condition requires that

$$\frac{L}{v} < \frac{\delta^2}{D}, \tag{19}$$

which gives a transverse Péclet number defined by

$$Pe_{trans} = \frac{\delta^2 v}{LD} > 1. \tag{20}$$

As a measure of the tendency to form longitudinal concentration gradients, the following inequality is more appropriate

$$\frac{L}{v} < \frac{L^2}{D}, \tag{21}$$

which implies a longitudinal Péclet number defined by

$$Pe_{long} = \frac{Lv}{D} > 1. \tag{22}$$

For an equant pore where $L = \delta$, Eq. (20) is equivalent to Eq. (22).

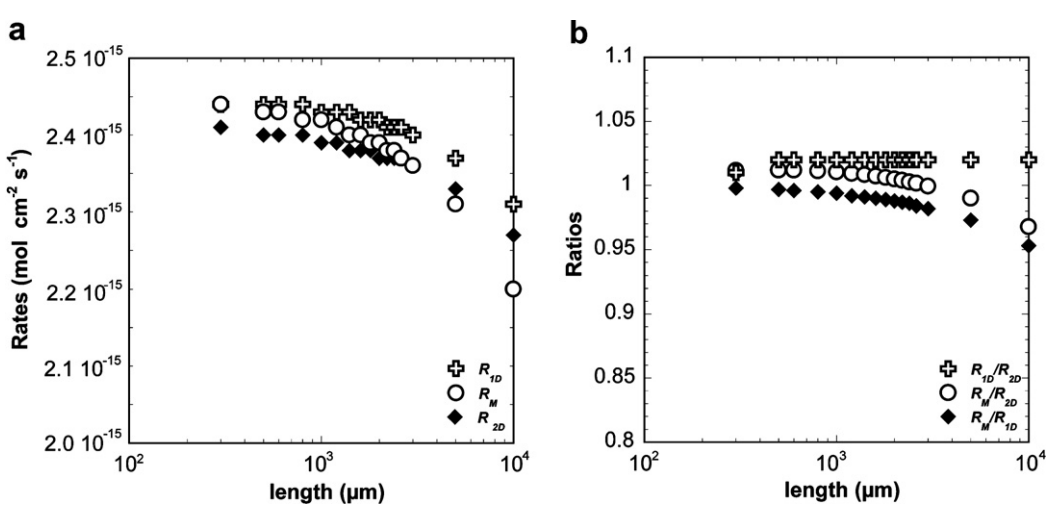

Fig. 10. (a) Overall steady-state plagioclase dissolution rates calculated as a flux-weighted average at the fracture outlet from the three models as a function of fracture length: the Poiseuille Flow model (R_{2D}), the 1D Plug Flow Reactor model (R_{1D}), and the Well-Mixed Reactor model (R_M). (b) The comparison of steady-state rates from different models. Rates from all three models look similar, with ratios close to unity. However, the effects of longitudinal mixing (R_M/R_{1D}) are larger than that of transverse mixing (R_{1D}/R_{2D}).

As an example, Fig. 11 shows values of Péclet number under various pore or fracture length and flow conditions, calculated with a diffusion coefficient of 8.57×10^{-5} cm^2/s for hydrogen ion concentration. It is interesting to notice that in the longitudinal direction, the more rapid the flow and the longer the fracture or pore, the larger the Péclet number (Fig. 11a). Thus, longer fractures increase the possibility of developing concentration gradients (and thus scale-dependent reaction rates) in the longitudinal direction. From Eq. (20) it is apparent that in the transverse direction, the Péclet number increases with decreasing pore or fracture length (Fig. 11b), indicating that transverse mixing becomes complete with a long enough flow path. This is why the rate discrepancy is largest for fractures with short lengths (Fig. 8). For flow velocities encountered under natural conditions (typically slower than 0.001 cm/s) and pores or fractures are less than 1 millimeter in length, the Péclet number is less than 1, meaning mixing in both longitudinal and transverse directions is complete. This is consistent with the results presented above.

The second condition means that the time scale of reaction is comparable to that of advection ($\tau_{react} \approx \tau_{ad}$). Here we define a dimensionless number $\eta = \tau_{react}/\tau_{ad}$. Large η values mean that the reaction rates are slow and significant changes in aqueous concentrations do not occur over the advective length scale. Under these conditions, the reaction rates within the pore or fracture are uniform and no scaling effects develop. Small η values mean that the reaction is fast relative to the rate of advective transport and that the reaction either reaches equilibrium or goes to completion over the length scale considered. Under these conditions the reaction kinetics become irrelevant. Only when the reaction rate and the advection rate are comparable can aqueous concentration gradients develop and scaling effects become significant, as shown in Fig. 5.

Although dimensionless numbers comparing the diffusion rate and reaction rate have been defined for a single component system (Lasaga, 1986; Casey, 1987; Murphy et al., 1989), rigorous comparison between advection and reaction for a multicomponent reaction system remains challenging due to the nonlinear dependence of the reaction rates on aqueous concentrations that typically vary in space. Nonetheless, a rough estimate can still be obtained. Consider that along the flow path we need a large enough change in aqueous concentrations so that spatial variations in reaction rates can develop. Let this change in concentration be a fraction of $C_{eq} - C_0$, where C_{eq} is the concentration at equilibrium in units of mol/L, and C_0 is the inflow concentration in mol/L. Here we define the dimensionless number η as follows:

$$\eta = \frac{1000\gamma(C_{eq} - C_0)v}{LR_a}, \tag{23}$$

where the factor of 1000 is used to convert the units of C_{eq} and C_0 from mol/L to mol/m^3, γ is a fraction that varies from 0 to 1, with the term $\gamma(C_{eq} - C_0)$ indicating the change in average aqueous concentration that is large enough to create gradients, v is the average flow velocity (m/s), L is the characteristic length of the system (m), and R_a is the average or bulk dissolution rate determined by the reaction rate law and the average aqueous concentrations (mol/m^2/s). For example, for calcite dissolution under far from equilibrium conditions in a slightly acidic solution where the rate depends only on pH, R_a is given by the first term on the right hand side of the *Rate* in Eq. (4). With this, Eq. (23) becomes

$$\eta = \frac{1000\gamma(C_{eq} - C_0)v}{Ak_1 a_{H^+} L}, \tag{24}$$

Here A is surface area in the units of m^2/m^3 pore fluid. Under close to equilibrium conditions, the affinity term will also need to be included. The value of η parameter depends on the designated γ value, the solubility of the mineral, the average concentrations of aqueous species that affect the reaction rate, the reaction rate constant, the reactive surface area, as well as the flow velocity and characteristic length.

The choice of γ, the fractional approach to equilibrium (or reaction completion), is somewhat arbitrary and requires insight into the characteristics of the geochemical

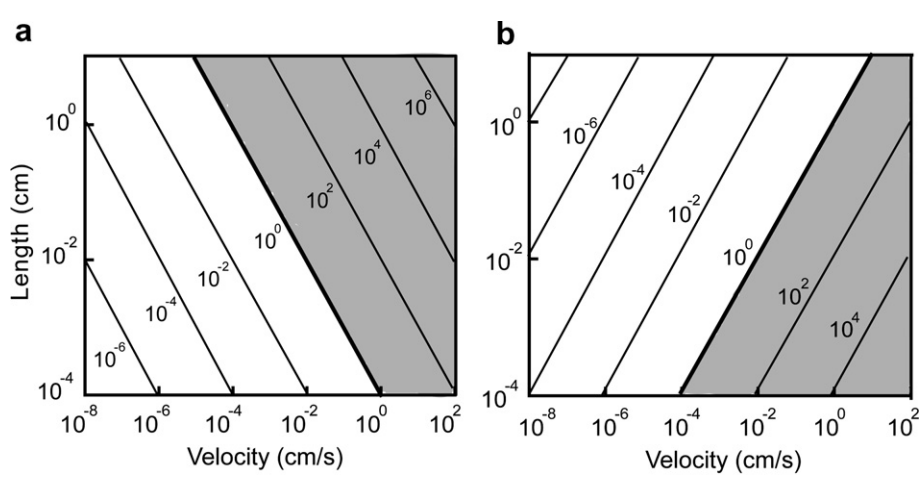

Fig. 11. Péclet number as a function of pore size and average flow velocity. (a) Péclet number defined in the longitudinal direction or assuming a equidimensional pore (Eq. (22)). (b) Péclet number in the transverse direction for a fracture (Eq. (20)) for an aperture of 100 μm. The conditions where $Pe > 1$ are shown in gray.

system. Relatively small fractional changes in concentration may be significant, as is shown by the following example. For the case of calcite dissolution in a 100 μm equant pore with a flow velocity of 0.1 cm/s shown in Fig. 4, pH increases to 6.4 at the pore wall while pH remains 5.0 at the center of the pore. Close to the pore wall, therefore, the Ca^{2+} concentration reaches as high as 20 μM, while the Ca^{2+} concentration within most of the pore remains very low. This leads to an average Ca^{2+} of 4.6 μM. Assuming a solubility of 316 μM based on stoichiometric dissolution of calcite, this average concentration corresponds to a γ value of 0.014. For a pore of length 1000 μm at a higher flow velocity of 1.0 cm/s where the rate discrepancy is largest, as shown in Figs. 5 and 6, a γ value of 0.001 is appropriate. Under far from equilibrium conditions, such a low γ value is due to the strong dependence of calcite dissolution rate on pH, small changes in which can have a significant effect on the rate. In the situation where the rate is independent of pH, the concentration dependence of the rate law comes from the approach to equilibrium, or the "affinity term" (e.g., quartz dissolution under acidic to neutral pH conditions). In this case, only changes in concentration relatively close to equilibrium are relevant, which would require a much larger γ value.

As an example, here we calculate values of η parameter under various flow and fracture length conditions for both calcite and plagioclase dissolution. Based on the discussion above, a γ value of 0.001 is used for both reactions as an indicator of where significant concentration gradients begin to develop. For a parallel-sided fracture with an aperture of 100 μm, the reactive surface A is 2×10^4 m^2/m^3 pore fluid. For the case of calcite dissolution, we assume that the fluid flowing in to the fracture has a pH of 5 and a pCO_2 of 3.14×10^{-4} bars, so an average activity of hydrogen ion 5×10^{-6} (half of the inflow value) is assumed. Using these parameters, a series of η values can be calculated for different average flow velocities and fracture length, as shown in Fig. 12a. Only at values of η close to 1 can significant concentration gradients develop and produce a scale dependence to the dissolution rates. Due to the rapid dissolution rate of calcite, η values are orders of magnitude smaller than unity under most conditions. At higher values of η, there is insufficient reaction to produce a concentration gradient. This leads to a narrow range of flow velocity and fracture length occupying the low right corner of the figure, where concentration gradients are likely to develop.

Calculating values for η for plagioclase is more difficult because of the additional constraints needed to calculate a solubility. The solubility of plagioclase depends on pH and concentrations of various species, including Na^+, Ca^{2+}, SiO_2(aq), and Al^{3+}. Here we assume that Ca^{2+} activity is constrained by equilibrium with calcite assuming stoichiometric dissolution, SiO_2(aq) by equilibrium with quartz, and Al^{3+} by equilibrium with $Al(OH)_3$(am). At a pH of 7.5, this gives a $C_{eq,Na}$ of 3×10^{-3} M. Replacing the term R_m in Eq. (23) with the aluminum inhibition rate law given in Eq. (6), we obtain η values at a variety of flow velocities and fracture lengths as shown in Fig. 12b. Due to its much slower dissolution rate and different solubility, the η values are orders of magnitude larger than calcite under similar flow and fracture length conditions. However, it should be noted that an η value close to unity is only one of the conditions for a scale dependence to develop. It is also necessary that the regions in parameter space where η values are close to unity in Fig. 12 must overlap with areas where $Pe \geqslant 1$ in Fig. 11 for concentration gradients to develop. For calcite dissolution in a 100 μm equant pore, overlap of $Pe > 1$ (Fig. 11a) and η in the vicinity of unity (for example, 10^{-3} to 10^3) occur when flow velocities are between approximately 0.1 and 1000 cm/s, as shown in Fig. 13a. This is consistent with the results presented in Figs. 5 and 6. For pores or fracture developed in plagioclase, it is only in pores or fractures close to 1 cm in length that the two conditions overlap. For both mineral dissolution reactions there is no overlap area for pores or fractures of length between 10 and 1000 μm under natural conditions where flow is mostly slower than 10^{-3} cm/s. For both minerals, the area of overlap ($Pe > 1$ and η values close to unity) increases with increasing fracture or pore length.

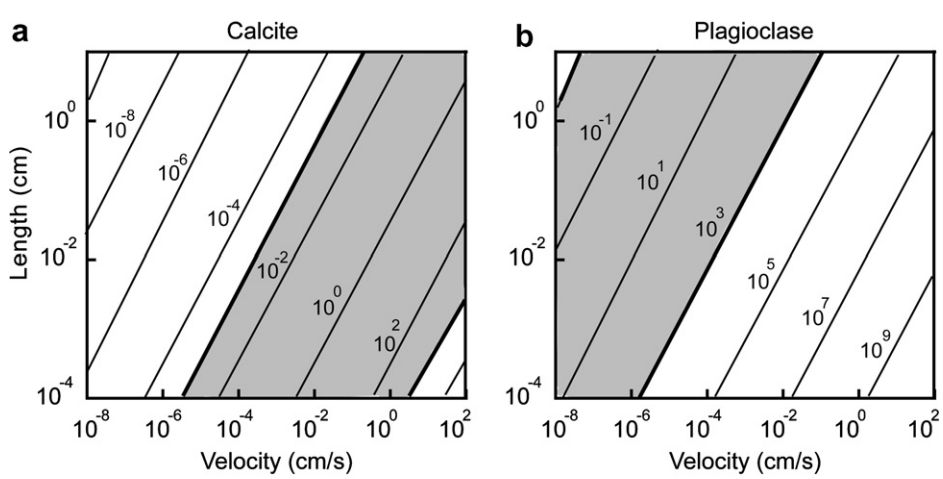

Fig. 12. Values of dimensionless number, η, as a function of average flow velocity and fracture length for calcite (a) and plagioclase (b). The gray area is where η values are between 10^{-3} and 10^3.

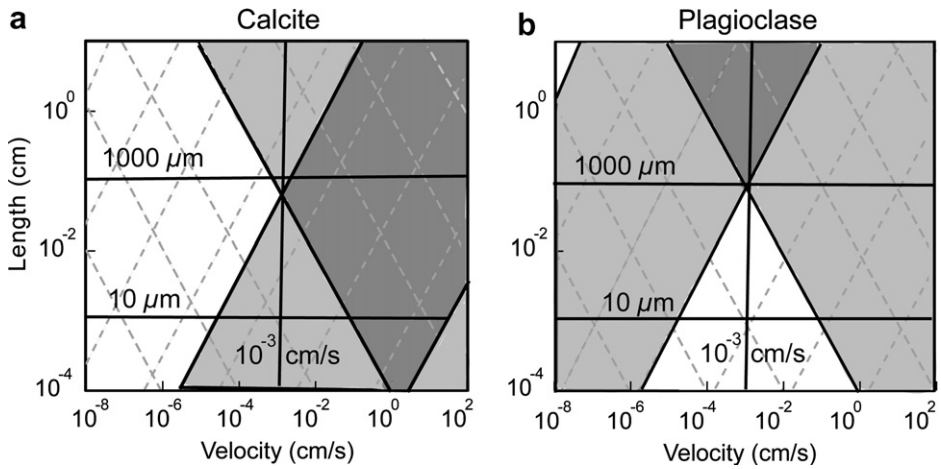

Fig. 13. Conditions for scaling effects (overlap areas of $Pe > 1$ and η values close to unity shown as shaded in dark gray) for calcite (a) and plagioclase (b).

6. DISCUSSION

The results presented here demonstrate that a scale dependence to mineral dissolution rates, leading potentially to a discrepancy between laboratory and field rates, arises when large concentration gradients develop. Where such conditions arise, the situation is inherently different from the well mixed laboratory conditions where most mineral reaction rates are measured. This implies that it is only in transport regimes where homogeneous concentration fields form that laboratory-measured reaction rates be used directly. This is consistent with findings from other studies at other spatial scales (Mo and Friedly, 2000; Meile and Tuncay, 2006; Mohamed et al., 2006) where it was demonstrated that relatively fast reaction kinetics combined with low advection and diffusion rates can generate a scaling effect, and thus a discrepancy between lab and field rates.

The above results are based on idealized single pore and single fracture models. Natural pores often have quite different characteristics than the idealized pore investigated in this work, including irregular shapes, rough surfaces, a larger number of openings (Lindquist et al., 2000), and heterogeneous solid phase compositions. However, our conclusion that at the pore scale the system remains well-mixed (thus avoiding the development of a scale dependence) is probably still valid with these characteristics. The cylindrical pore proposed in this work, with only two openings and smooth mineral surfaces, represents an extreme condition with a minimum extent of mixing. The characteristics of natural pores, such as irregular shape, a larger number of openings, and rough mineral surfaces, would all likely increase the extent of mixing and therefore reduce the discrepancy between the natural (field) and laboratory rates due to incomplete mixing. In the case where reactive minerals are distributed heterogeneously within a pore, a scale dependence is still considered unlikely because of the slow flow rates and the effectiveness with which molecular diffusion homogenizes the local aqueous phase at this scale.

Although under natural conditions the dependence of mineral dissolution rates on scale is considered to be negligible at the scale of single pores and fractures, at larger spatial scales these effects are expected to become more significant, as can be observed in Fig. 13 where larger regions of overlap develop with increasing fracture length. The characteristic time for diffusion or dispersion to homogenize a concentration field, defined as L^2/D, is proportional to the square of the length scale and therefore increases rapidly with increasing spatial scale. As such, at larger spatial scales the conditions for rate discrepancy to appear are more easily encountered. Field measurements of dissolution rates are often carried out at much larger spatial scales than the pore scale (Zhu, 2005), which may provide an explanation for the consistent emergence of the scaling issue and lab-field rate discrepancies.

7. CONCLUSIONS

In summary, we examined the effects of flow and transport processes on mineral dissolution kinetics in single pores and fractures. Laboratory-measured reaction kinetics were coupled with Poiseuille flow and advective and diffusive transport to unravel some of mechanisms that might contribute to a scale dependence of the dissolution rates, and thus to a discrepancy between laboratory and field rates. The simulations were intended to identify the conditions under which such a rate discrepancy becomes significant at the single pore scale by comparing the results with a well-mixed pore where pore-scale transport processes are ignored.

Simulations of reactive transport within single pores show that a scale dependence to mineral dissolution rates arise primarily as a result of the formation of concentration gradients at this scale, which develop due to comparable rates of reaction and advective transport *and* incomplete mixing via molecular diffusion. Thus, the magnitude of the reaction rates plays a large role in determining the scaling behavior of reaction rates. For calcite dissolution, the discrepancy in rates between a natural (represented by a Poiseuille Flow model) and well-mixed pore becomes significant at flow velocities between 0.1 and 1000 cm/s, while the discrepancy is negligible at slower or faster flow rates. In

the case of plagioclase dissolution and iron mineral reductive dissolution, the rates are too slow to register a significant effect at the higher flow rates where molecular diffusion does not dominate. Under natural conditions where flow velocities are typically lower than 0.001 cm/s, molecular diffusion homogenizes the concentration fields, and even the scale dependence of calcite dissolution rates disappears. Thus, we conclude that for single pores, the discrepancy between the rate determined with the flux-weighted average at the pore outlet and the rate calculated assuming complete mixing is negligible. The single pore or fracture, therefore, behaves effectively as a well-mixed reactor. We conclude therefore that the widely cited discrepancy between laboratory and field rates cannot be attributed to processes taking place at the single pore scale.

With single fractures, we also examined the effects of length scale on the rate discrepancy and the effects of transverse and longitudinal mixing. Again, the magnitude of the reaction rates plays a large role in how important the discrepancy between a natural pore and its well-mixed analogue is. For fast calcite dissolution, the effects of transverse mixing are more important than those due to longitudinal mixing, because the fast dissolution rates lead to large differences in concentration between the fracture wall and center. Discrepancies in rate between a fracture represented with Poiseuille Flow and realistic diffusion and a fracture within which complete mixing is assumed decrease with increasing fracture length in the case of calcite due to the combined effects of slower reaction rates downstream as the pH rises and as a result of the increased extent of mixing via molecular diffusion. For fractures of a length of more than 0.2 cm differences in the rates determined with the two approaches (Poiseuille Flow and complete mixing) are negligible. For plagioclase and iron hydroxide, although longitudinal mixing is more important, scaling effects are negligible within a spatial scale of one centimeter because of the slow rate of the dissolution reactions. However, at length scales >1 cm, the Poiseuille Flow and 1D Plug Flow models begin to diverge from rates calculated assuming complete mixing, suggesting that the discrepancy may become increasingly important at larger scales.

The modeling results presented above are consistent with the time scale analysis, which quantifies approximately the conditions under which concentration gradients, and thus scaling effects, may develop. The analysis shows that scaling effects arise under two necessary conditions, both of which need to be satisfied. One is that the time scale of advection must be smaller than that of diffusion, which requires that the Péclet number to be larger than unity. The second is that the time scales for advection and reaction must be comparable, with a ratio of the two time scales within about several orders of magnitude of unity, so that the extent of reaction is large enough to develop significant concentration gradients.

ACKNOWLEDGMENTS

Funding was provided to the Center for Environmental Kinetics Analysis (CEKA) by the U.S. Department of Energy's Environmental Remediation Science Program as part of a joint NSF-DOE Environmental Molecular Science Institute at Pennsylvania State University. Additional funding was provided by the Laboratory-Directed Research and Development program at Lawrence Berkeley National Laboratory. We are grateful for the review of an early version of the manuscript provided by Dr. Donald DePaolo. We thank Eric H. Oelkers, Pierre Regnier, and two anonymous reviewers for constructive reviews that have greatly improved the manuscript. This work was supported by the Director, Office of Science, Office of Biological and Environmental Research of the U.S. Department of Energy under Contract No. DE-AC02-05CH11231 to Lawrence Berkeley National Laboratory.

REFERENCES

Acharya R. C., Van der Zee S. and Leijnse A. (2005) Transport modeling of nonlinearly adsorbing solutes in physically heterogeneous pore networks. *Water Resour. Res.* **41**(2).

Alekseyev V. A., Medvedeva L. S., Prisyagina N. I., Meshalkin S. S. and Balabin A. I. (1997) Change in the dissolution rates of alkali feldspars as a result of secondary mineral precipitation and approach to equilibrium. *Geochim. Cosmochim. Acta* **61**(6), 1125–1142.

Anbeek C. (1993) The effect of natural weathering on dissolution rates. *Geochim. Cosmochim. Acta* **57**(21-22), 4963–4975.

Anderson R. T., Vrionis H. A., Ortiz-Bernad I., Resch C. T., Long P. E., Dayvault R., Karp K., Marutzky S., Metzler D. R., Peacock A., White D. C., Lowe M. and Lovley D. R. (2003) Stimulating the in situ activity of Geobacter species to remove uranium from the groundwater of a uranium-contaminated aquifer. *Appl. Environ. Microbiol.* **69**(10), 5884–5891.

Appelo C. A. J., Van der Weiden M. J. J., Tournassat C. and Charlet L. (2002) Surface complexation of ferrous iron and carbonate on ferrihydrite and the mobilization of arsenic. *Environ. Sci. Technol.* **36**(14), 3096–3103.

Bear J. (1972) *Dynamics of Fluids in Porous media*. Dover Publications, Inc., NY.

Berner R.A. (1978) Rate control of mineral dissolution under earth surface conditions. *Am. J. Sci.* **278,** 1235–1252.

Berner R. A. (1995) Chemical weathering and its effect on atmospheric CO_2 and climate. *In Chemical Weathering Rates of Silicate Minerals* **vol. 31**, 565–583.

Berner R. A. and Berner E. K. (1997) Silicate weathering and climate. In *Tectonics, Uplift and Climate Change* (ed. W. Ruddiman), pp. 353–365. Tectonics, Uplift and Climate Change. Plenum, NY.

Blum A. E. and Stillings L. L. (1995) Feldspar dissolution kinetics. In *Chemical Weathering Rates of Silicate Minerals*, vol. 31 (eds. A. F. White and S. L. Brantley). Mineralogical Society of America, pp. 291–351.

Burch T. E., Nagy K. L. and Lasaga A. C. (1993) Free energy dependence of albite dissolution kinetics at 80 °C and pH 8.8. *Chem. Geol.* **105**(1-3), 137–162.

Carroll S. A. and Knauss K. G. (2005) Dependence of labradorite dissolution kinetics on CO_2(aq), Al(aq), and temperature. *Chem. Geol.* **217**(3–4 SPEC. ISS.), 213–225.

Casey W. H. (1987) Heterogeneous kinetics and diffusion boundary-layers—the example of reaction in a fracture. *J. Geophys. Res.—Solid Earth Planets* **92**(B8), 8007–8013.

Chorover J., Choi S. K., Amistadi M. K., Karthikeyan K. G., Crosson G. and Mueller K. T. (2003) Linking cesium and strontium uptake to kaolinite weathering in simulated tank waste leachate. *Environ. Sci. Technol.* **37**(10), 2200–2208.

Chou L., Garrels R. M. and Wollast R. (1989) Comparative study of the kinetics and mechanisms of dissolution of carbonate minerals. *Chem. Geol.* **78**, 269–282.

Coates J. D. and Anderson R. T. (2000) Emerging techniques for anaerobic bioremediation of contaminated environments. *Trends Biotechnol.* **18**(10), 408–412.

Daugherty R. L. and Franzini J. B. (1965) *Fluid Mechanics with Engineering Applications*. McGraw-Hill, NY.

Dibble W. E. and Tiller W. A. (1981) Nonequilibrium water–rock interactions. 1. Model for interface-controlled reactions. *Geochim. Cosmochim. Acta* **45**(1), 79–92.

Dzombak D. A. and Morel F. M. M. (1990) *Surface complexation modeling*. John Wiley and Sons, NY.

Freeze R. A. and Cherry J. A. (1979) *Groundwater*. Prentice Hall, Inc., Englewood Cliffs, NJ.

Gelhar L. W., Welty C. and Rehfeldt K. R. (1992) A critical-review of data on field-scale dispersion in aquifers. *Water Resour. Res.* **28**(7), 1955–1974.

Giambalvo E. R., Steefel C. I., Fisher A. T., Rosenberg N. D. and Wheat C. G. (2002) Effect of fluid-sediment reaction on hydrothermal fluxes of major elements, eastern flank of the Juan de Fuca Ridge. *Geochim. Cosmochim. Acta* **66**(10), 1739–1757.

Hellmann R. and Tisserand D. (2006) Dissolution kinetics as a function of the Gibbs free energy of reaction: an experimental study based on albite feldspar. *Geochim. Cosmochim. Acta* **70**(2), 364–383.

Hwang, II, S. and Powers S. E. (2003) Lognormal distribution model for estimating soil water retention curves for sandy soils. *Soil Sci.* **168**(3), 156–166.

Jaisi D. P., Dong H. L. and Liu C. X. (2007) Influence of biogenic Fe(II) on the extent of microbial reduction of Fe(III) in clay minerals nontronite, illite, and chlorite. *Geochim. Cosmochim. Acta* **71**(5), 1145–1158.

Khaleel R. and Heller P. R. (2003) On the hydraulic properties of coarse-textured sediments at intermediate water contents. *Water Resour. Res.* **39**(9).

Khaleel R. and Relyea J. F. (2001) Variability of Gardner's alpha for coarse-textured sediments. *Water Resour. Res.* **37**(6), 1567–1575.

Knauss K. G., Johnson J. W. and Steefel C. I. (2005) Evaluation of the impact of CO_2, co-contaminant gas, aqueous fluid and reservoir rock interactions on the geologic sequestration of CO_2. *Chem. Geol.* **217**, 339–350.

Lasaga A. C. (1986) Metamorphic reaction-rate laws and development of isograds. *Mineral. Mag.* **50**(357), 359–373.

Lasaga A. C. (1998) *Kinetic theory in the earth sciences*. Princeton University Press, NJ.

Li L., Peters C. A. and Celia M. A. (2006) Upscaling geochemical reaction rates using pore-scale network modeling. *Adv. Water Resour.* **29**(9), 1351–1370.

Li L., Peters C. A. and Celia M. A. (2007) Effects of mineral spatial distribution on reaction rates in porous media. *Water Resour. Res.* **43**(1). doi:10.1029/2005WR004848.

Lindquist W. B., Venkatarangan A., Dunsmuir J. and Wong T. F. (2000) Pore and throat size distributions measured from synchrotron X-ray tomographic images of Fontainebleau sandstones. *J. Geophys. Res.—Solid Earth Planets* **105**(B9), 21509–21527.

Liu C. X., Kota S., Zachara J. M., Fredrickson J. K. and Brinkman C. K. (2001) Kinetic analysis of the bacterial reduction of goethite. *Environ. Sci. Technol.* **35**(12), 2482–2490.

Lovley D. R. (1993) Dissimilatory metal reduction. *Annu. Rev. Microbiol.* **47**, 263–290.

Lovley D. R. and Coates J. D. (1997) Bioremediation of metal contamination. *Curr. Opin. BioTechnol.* **8**(3), 285–289.

Maher K., DePaolo D. J. and Lin J. C. F. (2004) Rates of silicate dissolution in deep-sea sediment: In situ measurement using U-234/U-238 of pore fluids. *Geochim. Cosmochim. Acta* **68**(22), 4629–4648.

Maher K., Steefel C. I., DePaolo D. J. and Viani B. E. (2006) The mineral dissolution rate conundrum: insights from reactive transport modeling of U isotopes and pore fluid chemistry in marine sediments. *Geochim. Cosmochim. Acta* **70**(2), 337–363.

Malmstrom M. E., Destouni G., Banwart S. A. and Stromberg B. H. E. (2000) Resolving the scale-dependence of mineral weathering rates. *Environ. Sci. Technol.* **34**(7), 1375–1378.

Malmstrom M. E., Destouni G. and Martinet P. (2004) Modeling expected solute concentration in randomly heterogeneous flow systems with multicomponent reactions. *Environ. Sci. Technol.* **38**, 2673–2679.

Meile C. and Tuncay K. (2006) Scale dependence of reaction rates in porous media. *Adv. Water Resour.* **29**(1), 62–71.

Mo Z. and Friedly J. C. (2000) Local reaction and diffusion in porous media transport models. *Water Resour. Res.* **36**(2), 431–438.

Mohamed M. M. A., Hatfield K. and Hassan A. E. (2006) Monte Carlo evaluation of microbial-mediated contaminant reactions in heterogeneous aquifers. *Adv. Water Resour.* **29**(8), 1123–1139.

Morse J. W. and Arvidson R. S. (2002) The dissolution kinetics of major sedimentary carbonate minerals. *Earth Sci. Rev.* **58**(1-2), 51–84.

Murphy W. M., Oelkers E. H. and Lichtner P. C. (1989) surface reaction versus diffusion control of mineral dissolution and growth rates in geochemical processes. *Chem. Geol.* **78**, 357–380.

Newman J. S. (1991) *Electrochemical systems*. Prentice Hall, Englewood Cliffs, NJ.

Oelkers E. H. (1996) Physical and chemical properties of rocks and fluids for chemical mass transport calculations. In *Reactive Transport in Porous Media*, vol. 34 (eds. P. C. Lichtner, C. I. Steefel and E. H. Oelkers). The Mineralogical Society of America, pp. 131–191.

Oelkers E. H., Schott J. and Devidal J.-L. (1994) The effect of aluminum, pH, and chemical affinity on the rates of aluminosilicate dissolution reactions. *Geochim. Cosmochim. Acta* **58**(9), 2011–2024.

Plummer L. N., Wigley T. M. L. and Parkhurst D. L. (1978) The kinetics of calcite dissolution in CO_2–water systems at 5 degree C to 60 degree C and 0.0 to 1.0 atm CO_2. *Am. J. Sci.* **278**, 179–216.

Roden E. E. (2004) Analysis of long-term bacterial vs. chemical Fe(III) oxide reduction kinetics. *Geochim. Cosmochim. Acta* **68**(15), 3205–3216.

Roden E. E. and Urrutia M. M. (2002) Influence of biogenic Fe(II) on bacterial crystalline Fe(III) oxide reduction. *Geomicrobiol. J.* **19**(2), 209–251.

Roden E. E., Urrutia M. M. and Mann C. J. (2000) Bacterial reductive dissolution of crystalline Fe(III) oxide in continuous-flow column reactors. *Appl. Environ. Microbiol.* **66**(3), 1062–1065.

Roden E. E. and Zachara J. M. (1996) Microbial reduction of crystalline iron(III) oxides: influence of oxide surface area and potential for cell growth. *Environ. Sci. Technol.* **30**(5), 1618–1628.

Scheibe T. D., Fang Y., Murray C. J., Roden E. E., Chen J., Chien Y.-J., Brooks S. C. and Hubbard S. S. (2006) Transport and biogeochemical reaction of metals in a physically and chemically heterogeneous aquifer. *Geosphere* **2**(4). doi:10.1130/GES00029.1.

Spycher N. F., Sonnenthal E. L. and Apps J. A. (2003) Fluid flow and reactive transport around potential nuclear waste emplacement tunnels at Yucca Mountain, Nevada. *J. Contam. Hydrol.*, 653–673.

Steefel C. I. (2007) Geochemical kinetics and transport. In *Kinetics of Water–Rock Interaction* (eds. S. L. Brantley, J. D. Kubicki and A. F. White). Springer, New York, pp. 539–584.

Steefel C. I. (2008) *CrunchFlow User's Manual*. Lawrence Berkeley National Laboratory.

Steefel C. I., Carroll S., Zhao P. and Roberts S. (2003) Cesium migration in Hanford sediment: a multisite cation exchange model based on laboratory transport experiments. *J. Contam. Hydrol.* **67**(1-4), 219–246.

Steefel C. I., DePaolo D. J. and Lichtner P. C. (2005) Reactive transport modeling: an essential tool and a new research approach for the Earth sciences. *Earth Planet. Sci. Lett.* **240**, 539–558.

Steefel C. I. and Lasaga A. C. (1994) A coupled model for transport of multiple chemical species and kinetic precipitation/dissolution reactions with application to reactive flow in single phase hydrothermal systems. *Am. J. Sci.* **294**, 529–592.

Steefel C. I. and Lichtner P. C. (1998) Multicomponent reactive transport in discrete fractures: I. Controls on reaction front geometry. *J. Hydrol.* **209**(1-4), 186–199.

Steefel C. I. and MacQuarrie K. T. B. (1996) Approaches to modeling of reactive transport in porous media. In *Reactive Transport in Porous Media*, vol. 34 (eds. P. C. Lichtner, C. I. Steefel and E. H. Oelkers). The Mineralogical Society of America, pp. 83–130.

Steefel C. I. and Van Cappellen P. (1990) A new kinetic approach to modeling water-rock interaction: the role of nucleation, precursors, and Ostwald ripening. *Geochim. Cosmochim. Acta* **54**(10), 2657–2677.

Stefansson A. (2001) Dissolution of primary minerals of basalt in natural waters: I. Calculation of mineral solubilities from 0 °C to 350 ° C. *Chem. Geol.* **172**(3-4), 225–250.

Taylor G. I. (1953) The dispersion of soluble matter in a solvent flowing through a tube. *Proc. R. Soc. Lond. Ser. A* **219**, 196–203.

White A. F. (1995) Chemical weathering rates of silicate minerals in soils. In *Chemical Weathering Rates of Silicate Minerals*, vol. 31 (eds. A. F. White and S. L. Brantley). Mineralogical Society of America, pp. 407–461.

White A. F. and Brantley S. L. (1995) Chemical weathering rates of silicate minerals: an overview. In *Chemical Weathering Rates of Silicate Minerals*, vol. 31 (eds. A. F. White and S. L. Brantley). Mineralogical Society of America, pp. 1–22.

White A. F. and Brantley S. L. (2003) The effect of time on the weathering of silicate minerals: why do weathering rates differ in the laboratory and field? *Chem. Geol.* **202**(3-4), 479–506.

White A. F. and Peterson M. L. (1990) Role of reactive-surface-area characterization in geochemical kinetic-models. *ACS Symp. Ser.* **416**, 461–475.

Zhu C. (2005) In situ feldspar dissolution rates in an aquifer. *Geochim. Cosmochim. Acta* **69**(6), 1435–1453.

Zhu C., Blum A. E. and Veblen D. (2004) Feldspar dissolution rates and clay precipitation in the Navajo aquifer at Black Mesa, Arizona, USA. *Water–Rock Interact.*, 895–899.

Associate editor: Eric H. Oelkers